CHEMISTRY OF MATERIALS

Generating Ferromagnetic Kagomé Metal by Magnetic Phase Boundary Mapping in the YFe_6Ge_6–YCo_6Ge_6 System

Published as part of Chemistry of Materials special issue "In Memory of Prof. Francis DiSalvo".

Victoria M. Li, Milo Adams, and Michael Shatruk*

Cite This: *Chem. Mater.* 2025, 37, 247−254

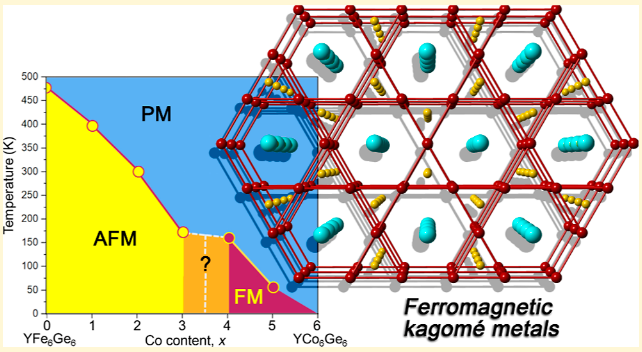

ABSTRACT: We demonstrate the possibility to generate itinerant ferromagnetism on a kagomé lattice by varying the structural parameters and valence electron concentration between antiferromagnetic YFe_6Ge_6 and paramagnetic YCo_6Ge_6. The substitution of Co for Fe in orthorhombic YFe_6Ge_6 leads to the gradual suppression of the antiferromagnetic ordering temperature in $YFe_{6-x}Co_xGe_6$. At a higher Co content, $x \geq 4$, ferromagnetic-like behavior is observed along with the change in the symmetry to the hexagonal YCo_6Ge_6-type structure. Finally, the magnetic ordering is completely suppressed in YCo_6Ge_6. Density-functional theory calculations reveal that the suppression of magnetic ordering is caused by the filling of 3d states in the band structure of these materials. This work suggests the pathway to discover new ferromagnetic kagomé metals by judicious variation of the electronic band structure via the control of valence electron concentration.

INTRODUCTION

Magnetic materials with kagomé-type lattices have long served as testbeds for investigation of competing magnetic ground states in the case of antiferromagnetic (AFM) exchange coupling between nearest-neighbor spins.[1−7] This situation, known as spin frustration, emerges from the impossibility of satisfying all pairwise AFM interactions simultaneously on a lattice composed of corner-sharing triangles. As a result, the system demonstrates a highly degenerate ground state that leads to such exotic phases as spin ice or spin liquid.[6−8] Recently, however, ferromagnetic (FM) metals with the kagomé arrangement of spins have gained a renewed interest due to their potential to exhibit intriguing topological properties,[9] which stem from the presence of both high- and low-dispersion bands in the electronic structure of such materials. As a result, unusual physical behaviors can emerge due to coupling between magnetic and transport properties.[10] Representative examples are given by the observation of massive Dirac fermions in Fe_3Sn_2,[11] a giant anomalous Hall effect in $Co_3Sn_2S_2$,[12] and multiple field-dependent magnetic states induced by spin-charge coupling in YMn_6Sn_6.[13,14]

Despite the extensive recent developments in the study of FM kagomé metals, the scope of materials exhibiting such a combination of properties is relatively small, as compared to AFM kagomé materials. This is not surprising, taking into account that FM materials, in general, are less common than AFM ones. This status quo notwithstanding, it has been established for some time that metallic magnets can be tuned between different magnetically ordered states, which are dictated by the electronic structure in the vicinity of the Fermi level (E_F).[15−17] Moreover, the preference for the FM or AFM ordering can be correlated to the type of orbital interactions between the moment-carrying atoms in such materials.[18−20] As an example, nonbonding interactions observed at E_F for elemental Cr metal lead to AFM ordering, while further filling of 3d orbitals leads to antibonding interactions at E_F in Fe, Co, and Ni and, as a consequence, stabilization of the FM state for these metals.[21]

Such considerations suggest that magnetic kagomé metals offer an excellent playground to search for new FM materials and, moreover, to discover new manifestations of anomalous properties caused by coupling between the spin and charge in the kagomé-type structures. In this vein, we argue that such anomalous properties can be encountered in the kagomé-lattice materials that exist at the borderline between the closely related structure types with different space-group symmetries.

Received: August 24, 2024
Revised: December 12, 2024
Accepted: December 13, 2024
Published: December 30, 2024

ACS Publications

https://doi.org/10.1021/acs.chemmater.4c02382

The competition between the structure types, along with the disparity in the magnetic properties of parent materials, might enhance the spin-charge coupling and lead to nontrivial magnetic structures manifested as noncollinear spin textures. Inspired by similar explorative approaches to thermoelectrics,[22] we dub this strategy "magnetic phase boundary mapping".

Among known families of kagomé-lattice metals, the systems with the general formula AT_6X_6 (A = electropositive metal, T = transition metal, and X = main-group element) offer a rich compositional landscape for exploring various combinations of properties and factors that impact those properties.[10] The four common structure types of these materials are hexagonal $MgFe_6Ge_6$ and YCo_6Ge_6 (space group *P*6/*mmm*) and orthorhombic $TbFe_6Sn_6$ and YFe_6Ge_6 (space group *Cmcm*).[23] The general crystal structure is shown in Figure 1a, where the flat kagomé layers of T atoms are separated by A and X atoms. The $MgFe_6Ge_6$- and $TbFe_6Sn_6$-type structures show an ordered arrangement of all atomic sites, while in the YCo_6Ge_6- and YFe_6Ge_6-type structures a partial disorder with vacancy formation is observed for the adjacent A and X sites that appear above each other when viewed in the direction perpendicular to the kagomé layers (the location of these sites is indicated with blue rectangles in Figure 1). These A and X sites exhibit correlated occupancies due to the unrealistically short nearest-neighbor distances between them. In certain cases, more complex superstructures can form due to vacancy ordering.[24] Thus, one can expect strong correlations between the crystal and electronic structure and magnetic properties of the AT_6X_6-type materials.

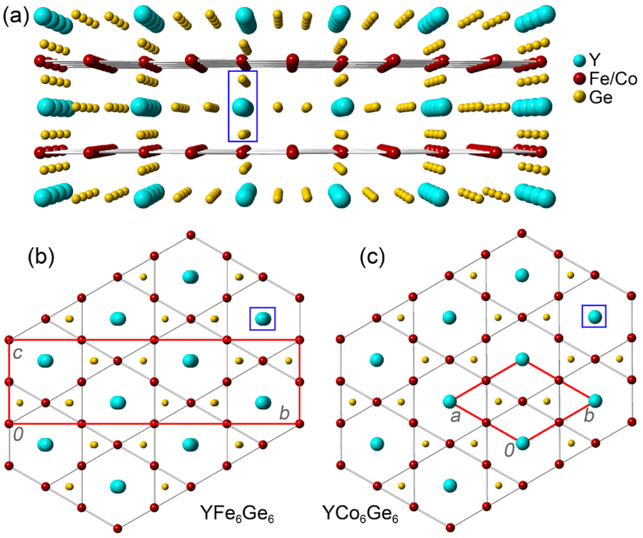

Figure 1. (a) Crystal structure of YT_6Ge_6 (T = Fe or Co), revealing the kagomé layers of transition-metal atoms (garnet) separated by layers of Ge (gold) and Y (cyan) atoms. The view perpendicular to the kagomé layers shows the larger orthorhombic unit cell of YFe_6Ge_6 (b) generated by a slight distortion of the hexagonal structure of YCo_6Ge_6 (c). The unit cells are indicated with solid red lines. The blue rectangle in each panel indicates the location of disordered Y and Ge atoms with correlated site occupancies due to prohibitively close Y−Ge nearest-neighbor distances.

Herein, we demonstrate the targeted discovery of kagomé metals with an enhanced FM response in the system YFe_6Ge_6−YCo_6Ge_6. The parent compounds exhibit AFM ordering at 487 K[25] and solely paramagnetic (PM) behavior,[26] respectively. YCo_6Ge_6 crystallizes in the hexagonal space group *P*6/*mmm*, while YFe_6Ge_6 exhibits a slight orthorhombic distortion that leads to the space group *Cmcm* (Figure 1).[27] We set out to investigate how the change from orthorhombic to hexagonal symmetry might impact the magnetic properties of the underlying material. As will be shown below, the gradual substitution of Co for Fe suppresses the AFM ordering temperature in $YFe_{6-x}Co_xGe_6$, until FM-like ordering, which substantially higher total magnetization, emerges for phases with $x > 3$ and disappears at the highest Co content.

■ MATERIALS AND METHODS

Starting Materials. Yttrium metal rod (>99.9%) was obtained from Beantown Chemical and filed to powder immediately before use. Powders of cobalt (99.998%, 22 mesh) and germanium (99.999%, 100 mesh) were obtained from Thermo Scientific, while the iron powder (99.9%, > 10 μm) was obtained from Aldrich. The iron, cobalt, and germanium powders were additionally purified by being heated under a flow of H_2 gas at 773 K for 5 h. All manipulations during sample preparation were carried out in an argon-filled drybox (content of O_2 < 0.2 ppm).

Synthesis. Samples of $YFe_{6-x}Co_xGe_6$ (x = 0.0, 1.0, 2.0, 3.0, 4.0, 5.0, and 6.0) were prepared by arc-melting pelletized stoichiometric mixtures of elements, with the total mass of ∼0.3 g for each sample. Each ingot was flipped and remelted 3−4 times to achieve better homogeneity. The obtained ingots were sealed under vacuum ($<10^{-4}$ mbar) in fused silica ampules of 10 mm inner diameter, annealed at 900 °C for 4 days, and cooled to room temperature (r.t.) by switching off the furnace. Two other series of samples were prepared for the sake of comparison, using different thermal treatments; one of them was cooled from 900 °C to room temperature (rt) at 8.75 °C/h, while the other was ice-quenched. The samples were ground to fine powders and briefly (∼2 h) washed with dilute aqueous HCl (1:1 v/v) to remove a minor Y_2O_3 impurity. The phase purity of the samples was confirmed by powder X-ray diffraction (PXRD).

Powder X-ray Diffraction. The PXRD measurements were carried out at rt using a Panalytical X'Pert Pro diffractometer with an X'Celerator detector or a Rigaku SmartLab diffractometer with a Lynxeye detector, both equipped with a Cu Kα radiation source (λ = 1.54187 Å). Each pattern was recorded in the 2θ range from 10° to 80° with a step of 0.02° and a total collection time of 1 h. The data analysis was performed with HighScore Plus.[28] The unit cell parameters and volume were determined by whole−pattern profile fitting using the Pawley profile function.

Physical Property Measurements. Energy-dispersive X-ray (EDX) elemental analysis was carried out on a JEOL JSM-IT800 scanning electron microscope with a field-emission electron gun operating under an accelerating potential of 20 kV. Several areas of each powder sample were probed to determine statistically averaged compositions. Magnetic studies were performed on powder samples using a magnetic property measurement system (MPMS-XL or MPMS-3, Quantum Design) equipped with a superconducting quantum interference device. Direct current magnetic susceptibility was measured in zero-field-cooled (ZFC) and field-cooled (FC) modes in the 5−400 K temperature range, with an applied field of 100 Oe. Hysteresis loops were recorded at 1.8 K, with the applied field varied from −70 to +70 kOe.

Quantum-Chemical Calculations. Density functional theory (DFT) calculations based on the projector augmented-wave method[29] were performed with the Vienna Ab initio Software Package (VASP).[30,31] A Perdew−Burke−Ernzerhof (PBE) exchange−correlation potential[32] was applied for the generalized gradient approximation (GGA) calculations. Integrations over the reciprocal unit cells were performed with a 5 × 3 × 11 *k*-point mesh and a 7 × 7 × 5 *k*-point mesh in the irreducible wedge of the orthorhombic and hexagonal Brillouin zones, respectively. The interatomic crystal orbital Hamilton population (COHP) analyses were performed with LOBSTER,[33] using Y-4d/4p/5s, Co/Fe-3d/4s, and Ge-4s/4p orbitals as a basis set. Orthorhombic unit cells in the *Cmcm* space group were

Table 1. Summary of Room-Temperature Unit Cell Parameters and Magnetic Properties of $YFe_{6-x}Co_xGe_6$

compound	Fe/Co ratio from EDX	symmetry	a (Å)	b (Å)	c (Å)	V/f.u. (Å^3)[a]	T_C or T_N (K)	M_{max} (μ_B)[b]
YFe_6Ge_6 (lit.)[27]		ortho	8.116	17.672	5.120	183.59	487 (AFM)	
YFe_6Ge_6		ortho	8.131(6)	17.60(1)	5.131(3)	183.6(2)	>400 (AFM)[c]	
YFe_5CoGe_6	5.12(9):1.04(6)	ortho	8.075(3)	17.701(9)	5.123(2)	183.1(1)	~400 (AFM)[c]	0.13
$YFe_4Co_2Ge_6$	4.06(8):2.06(5)	ortho	8.045(9)	17.64(2)	5.129(6)	182.0(4)	301 (AFM)	0.06
$YFe_3Co_3Ge_6$[d]	3.07(4):3:03(4)	ortho	7.9803(8)	17.6761(9)	5.108(1)	180.13(4)	176 (AFM)	0.19
$YFe_3Co_3Ge_6$[d]	3.07(4):3:03(4)	hex	5.1030(7)		3.9902(9)	180.0(1)	176 (AFM)	0.19
$YFe_2Co_4Ge_6$	2.02(3):4.08(7)	hex	5.0911(9)		3.963(2)	177.9(2)	161 (FM)	0.89
$YFeCo_5Ge_6$	0.99(2):5.10(5)	hex	5.106(3)		3.931(3)	177.5(6)	60 (FM)	0.37
YCo_6Ge_6		hex	5.096(1)		3.918(2)	176.2(2)	PM	
YCo_6Ge_6 (lit.)[34]		hex	5.074		3.908	174.26	PM	

[a] The volume is given per formula unit (f.u.), to allow the direct comparison between the orthorhombic and hexagonal structures. [b] The maximum magnetization value observed under an applied magnetic field of 7 T. [c] The ordering temperature was either above or close to the highest temperature of 400 K accessible in our experiments. [d] The unit cell of $YFe_3Co_3Ge_6$ was refined in both hexagonal and orthorhombic settings.

relaxed from the structural data previously reported for YFe_6Ge_6.[25] The hexagonal unit cells in the $P6/mmm$ space group were relaxed from the published lattice parameters of YCo_6Ge_6,[34] but the disorder observed in this structure was simplified by using atomic positions of the ordered $MgFe_6Ge_6$ analogue.[34]

■ RESULTS AND DISCUSSION

Synthesis and Crystal Structures. Arc-melting stoichiometric mixtures of elements, according to the compositions $YFe_{6-x}Co_xGe_6$, followed by homogenizing annealing at 900 °C, afforded the desired samples contaminated with a minor impurity of Y_2O_3 (Figure S1). The latter was easily removed by treating the samples with dilute HCl (1:1 v/v) for 2 h (Figure S2), which also indicated that the target materials are acid-resistant. The EDX elemental analysis showed that the Fe/Co ratio was in good agreement with the nominal composition of all samples (Table 1).

The appearance of the Y_2O_3 impurity, most likely, stems from the slight nonstoichiometry of yttrium in these compounds. Indeed, it has been reported that one of the parent ternary compounds showed the composition $Y_{0.9}Co_6Ge_6$.[34] The slight deficiency of Y is confirmed by changes in the intensity of weak low-angle peaks in the PXRD patterns. As shown in Figure S3, the stoichiometric YFe_6Ge_6 shows nearly equal intensities of the (110) and (021) reflections, while the (310) reflection is notably stronger. The decrease in the occupancy of the Y site to 90% and then to 80% leads to a progressive decrease in the (110) intensity and an increase in the (021) intensity, which becomes comparable to the intensity of the (310) peak. The examination of the experimental PXRD patterns of $YFe_{6-x}Co_xGe_6$ (Figure S1) clearly reveals the similar intensities of the weak (021) and (310) peaks (observed around 20° and 34°, respectively) and the lack of any intensity for the (110) peak expected around 12°.

The analysis of the PXRD data revealed that the samples were isostructural with either YFe_6Ge_6 or YCo_6Ge_6, depending on the Fe/Co ratio (Figure 2). The samples with the higher Co content ($x = 4, 5$) showed PXRD patterns analogous to that of hexagonal YCo_6Ge_6, while the samples with the lower Co content ($x < 4$) showed PXRD patterns analogous to that of orthorhombic YFe_6Ge_6. At the lower Co content, a clear splitting of some peaks was observed due to symmetry lowering caused by the transition to the orthorhombic YFe_6Ge_6-type structure.

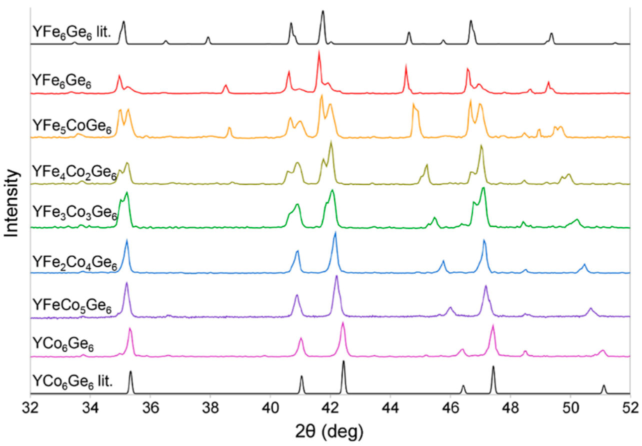

Figure 2. Selected fragment of the PXRD patterns of $YFe_{6-x}Co_xGe_6$, revealing the splitting of some diffraction peaks due to symmetry lowering from hexagonal ($x \geq 4$) to orthorhombic ($x \leq 3$).

The refinement of unit cell parameters from the PXRD patterns obtained for the parent ternary phases showed a good agreement with the literature data (Table 1 and Figure S4). Figure 3 shows the dependence of the unit cell parameters and volume on the Co content (x). For the sake of comparison, the unit cell of the hexagonal structures ($x \geq 4$) has been converted to the orthorhombic setting ($a_{ortho} = 2c_{hex}$, $b_{ortho} = 2\sqrt{3}\ a_{hex}$, $c_{ortho} = a_{hex}$), and the volume is given per formula unit (f.u.). The unit cell volume shows a nearly linear dependence on the Co content (Figure 3a), with the best-fit equation $V = -1.33(9)x + 184.0(3)$ (per f.u., $R^2 = 0.9678$). The decrease in the unit cell volume with the increasing Co content is in agreement with the smaller metallic radius of Co compared to that of Fe. The unit cell parameter perpendicular to the kagomé layers ($a_{ortho} = 2c_{hex}$) also shows a nearly linear dependence on x (Figure 3b), decreasing by ~4% between YFe_6Ge_6 and YCo_6Ge_6. Substantially smaller relative changes are observed for the unit cell edges parallel to the kagomé layers ($b_{ortho} = 2\sqrt{3}\ a_{hex}$ and $c_{ortho} = a_{hex}$). In these cases, the change in the parameters along the entire series is less than 1%.

The crystal structure of $YFe_3Co_3Ge_6$ is a borderline case, as the unit cell parameters could be refined in both the orthorhombic and hexagonal settings (Table 1). The parameter perpendicular to the kagomé layers was nearly the same in both settings (if the corresponding values of a_{ortho} and $2c_{hex}$ are compared), while a slight difference was observed in

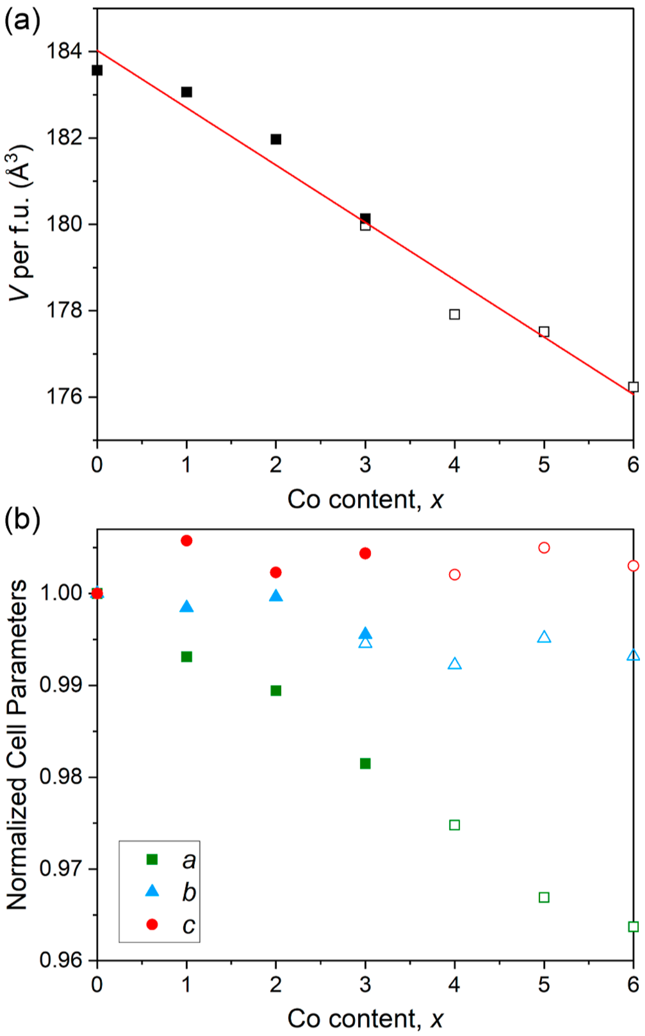

Figure 3. Unit cell volume per f.u. (a) and normalized unit cell parameters (b) for $YFe_{6-x}Co_xGe_6$. The cell parameters were normalized by dividing by the corresponding cell parameter of YFe_6Ge_6. All error bars are smaller than the symbol size. The solid red line in panel (a) shows a linear fit to the experimental data. The data refined in the orthorhombic and hexagonal settings are shown with closed and open symbols, respectively.

the parameters within the kagomé layer due to the higher number of degree of freedoms for unit cell fitting in the orthorhombic case. Nevertheless, the splitting of some peaks is still quite evident for this sample, suggesting that it belongs to the orthorhombic symmetry. We note that essentially the same trends in the unit cell parameters (Tables S1 and S2) and the transition from the orthorhombic to hexagonal symmetry around $x = 3$ (Figure S5 and S6) were observed for samples that were slowly cooled to rt or ice quenched from the homogenizing annealing temperature of 900 °C. Such thermal treatments, however, might lead to differences in finer details of the crystal structure, such as slightly different models of the Y/Ge site disorder and different amounts of strain/mosaicity of the samples. These effects will be explored in our future studies.

Overall, the evolution of the crystal structure along the series is associated with decreasing T−T distances both between and within the kagomé layers. The interlayer distance decreases substantially, from 4.060 Å in YFe_6Ge_6 ($a_{ortho}/2$) to 3.910 Å in YCo_6Ge_6 (c_{hex}), while the change in the intralayer T−T distance is much smaller, from 2.557 Å in YFe_6Ge_6 ($c_{ortho}/2$) to 2.537 Å in YCo_6Ge_6 ($a_{hex}/2$). These changes are accompanied by drastic changes in the magnetic behavior due to the increased filling of the 3d electronic states, as shown below.

Magnetic Properties. Magnetic properties were studied on powder samples of $YFe_{6-x}Co_xGe_6$. According to the literature reports, YFe_6Ge_6 exhibits AFM ordering of Fe moments at 487 K.[25] High-temperature AFM ordering is also observed in our measurements on the orthorhombic YFe_5CoGe_6, $YFe_4Co_2Ge_6$, and $YFe_3Co_3Ge_6$, which exhibit AFM ordering temperatures (T_N) of ~400, 301, and 176 K, respectively, as indicated by the maxima observed in the temperature dependence of magnetic susceptibility, χ (Figure 4a). The decrease in T_N with the increasing Co content suggests that electron doping has a destabilizing effect on the AFM-ordered ground state. The broad nature of these maxima might be indicative of disorder due to statistical occupancy of the 3d metal site by Fe and Co atoms, which can introduce some degree of glassiness due to the varying strength of magnetic exchange interactions in such a structure.

The hexagonal $YFe_2Co_4Ge_6$ sample exhibits drastically different behavior, with a clear signature of FM-like ordering revealed by field-cooled (FC) and zero-filed-cooled (ZFC) magnetic susceptibility measurements (Figure 4b). The ordering temperature (T_C) of 161 K was approximated from the intersection of two lines extrapolated from the nearly horizontal PM region and the rapidly increasing value of χ observed upon the FM-like ordering. The divergence between the ZFC and FC susceptibility curves also takes place at around the same temperature, supporting this T_C value.

Increasing the Co content even more, in $YFeCo_5Ge_6$, preserves FM-like behavior, although the T_C decreases to 60 K and a small dip in the magnetic susceptibility is observed below around 23 K, most likely, indicating substantial canting of magnetic moments and formation of a noncollinear spin texture. This notion is also supported by considering the observed maxima in the χ vs T curves for the $YFe_{6-x}Co_xGe_6$ samples. The maximum values of χ for the samples with $x \leq 3$ lie below 0.016 emu/mol, which is 3 orders of magnitude smaller than χ_{max} for $YFe_2Co_4Ge_6$ (~14.1 emu/mol) measured under the same magnetic field of 100 Oe. This value is also ~25 times larger than the maximum susceptibility of 0.58 emu/mol observed for $YFeCo_5Ge_6$. Thus, the FM component of magnetic ordering becomes most pronounced for the $YFe_2Co_4Ge_6$ composition.

To further explore the evolution from AFM to FM-like ordering in this series, we measured magnetization (M) as a function of magnetic field induction (B) at 5 K (Figure 5). The samples with $x \leq 3$ showed a linear dependence of M vs B and small maximum values of magnetization at ±7 T. Such observations are consistent with AFM nature of these materials. The slightly larger magnetization of $YFe_3Co_3Ge_6$ is also in agreement with the lower AFM ordering temperature observed for this sample (Table 1). Previous literature reported the magnetic structure of the parent compound, YFe_6Ge_6, as containing FM-coupled Fe moments in the kagomé layers, with antiparallel coupling between the layers leading to AFM ordering.[25,35] Based on the very low values of magnetization seen in YFe_5CoGe_6 and $YFe_4Co_2Ge_6$, one may hypothesize that their magnetic structure might be similar to that of YFe_6Ge_6, corresponding to the collinear AFM order. The higher M values observed for $YFe_3Co_3Ge_6$ might indicate the initial loss of collinearity, as this composition approaches

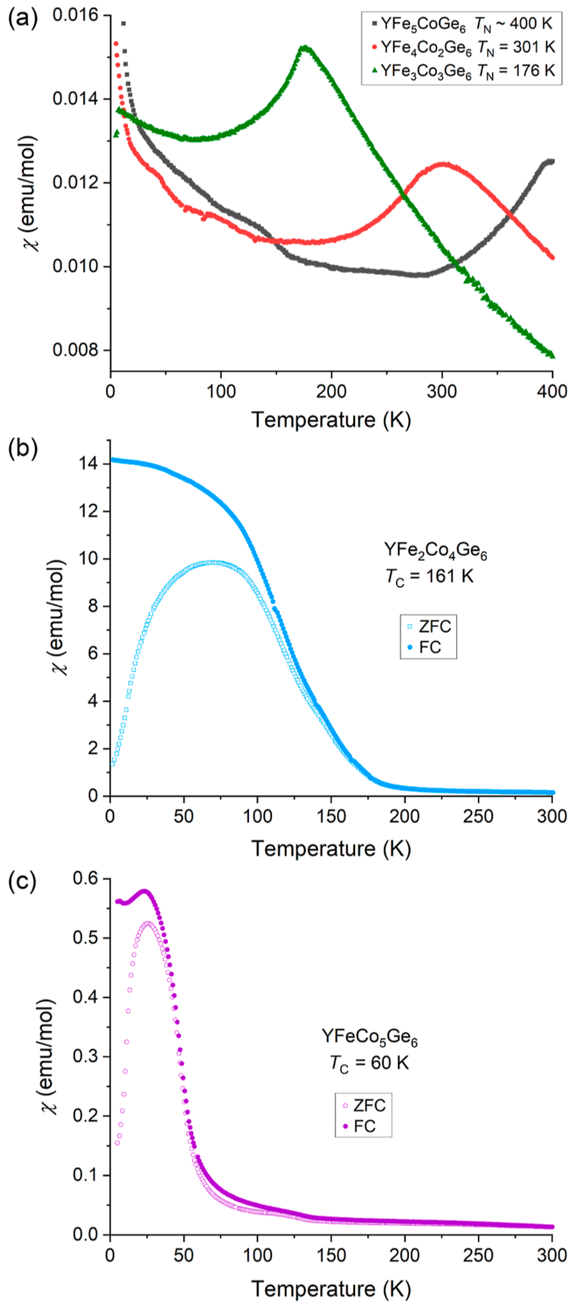

Figure 4. Temperature dependence of magnetic susceptibility for the powder samples of $YFe_{6-x}Co_xGe_6$ measured in the field-cooled (FC) regime (a) or in both field-cooled and zero-field cooled (ZFC) regimes (b,c) under an applied field of 100 Oe.

the borderline between the orthorhombic and hexagonal structure types (Figure 2).

The magnetic behavior of samples with a higher Co content is very different. Both $YFe_2Co_4Ge_6$ and $YFeCo_5Ge_6$ exhibit *S*-like magnetization hysteresis loops with negligible coercivity. The maximum *M* values observed are substantially larger than those for the Fe-rich samples, especially in the case of $YFe_2Co_4Ge_6$. Nevertheless, the saturation of magnetization, common for conventional FM materials, is not observed for these samples, suggesting that both compounds might show noncollinear spin textures with substantial uncompensated magnetic moments below T_C.[36] A precise understanding of such magnetic behavior requires investigation by neutron scattering methods, which we plan to pursue in the future.

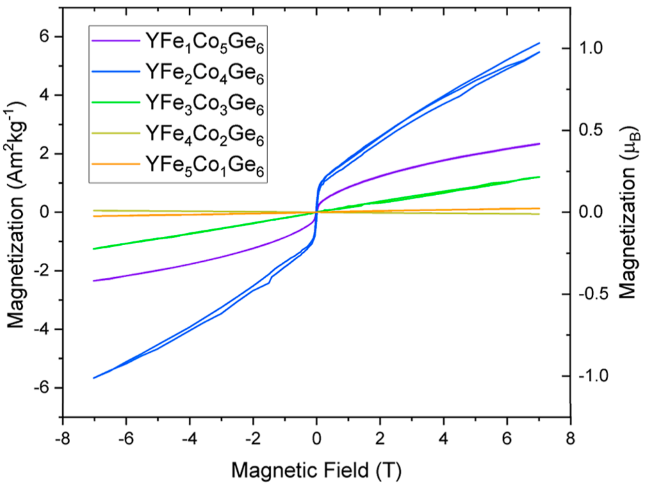

Figure 5. Field-dependent magnetization measured on the powder samples of $YFe_{6-x}Co_xGe_6$ at 5 K.

Electronic Structure Analysis. To further understand the evolution of magnetism with the change in the crystal structure parameters and valence electron concentration in the $YFe_{6-x}Co_xGe_6$ series, we studied the electronic band structure, density of states, and orbital interactions in the parent compounds, YFe_6Ge_6 and YCo_6Ge_6 by DFT calculations. The analysis was performed in both the $P6_3/mmm$ and $Cmcm$ space groups for each composition (Table 2), but the change in the space group symmetry did not have any pronounced impact on the character of the DOS or COHP near the Fermi level. Therefore, we discuss the electronic structures calculated for the experimentally established symmetries of YFe_6Ge_6 and YCo_6Ge_6.

Table 2. Calculated Values of the Stoner Criterion and the Total Energy Difference between the Spin-Polarized Magnetically Ordered (Magn) and Paramagnetic (PM) States for YFe_6Ge_6 and YCo_6Ge_6

Compound	YFe_6Ge_6	YCo_6Ge_6
	The Stoner Criterion, $J\cdot N(E_F)$	
Cmcm	2.55	0.46
P6/mmm	2.20	0.61
	$E_{Magn} - E_{PM}$ (meV/atom)	
Cmcm	−98.8 (FM) / −107.8 (AFM)	0.07 (FM) / 0 (AFM)
P6/mmm	−76.2 (FM) / −92.8 (AFM)	−0.06 (FM) / −0.04 (AFM)

Calculations without spin polarization revealed that the electronic density of states (*N*) of both structures (Figure 6) exhibits a large peak near the Fermi level (E_F), with the main contribution from the 3d orbitals of the transition metal. In the case of YFe_6Ge_6, the Fermi level crosses this peak (Figure 6a), leading to the electronic instability, according to Stoner.[37] Itinerant magnetic ordering can be expected when the Stoner criterion, defined as the product of $N(E_F)$ by the exchange coupling constant (J), exceeds 1.[20] The value of J can be approximated by the values reported for elemental 3*d* metals.[38] The calculations of the $J\cdot N(E_F)$ product for YFe_6Ge_6 (Table 2) show that the Stoner criterion is satisfied, conducive to spin polarization of the electronic structure and ensuring magnetic ordering, in agreement with the experimental observations.

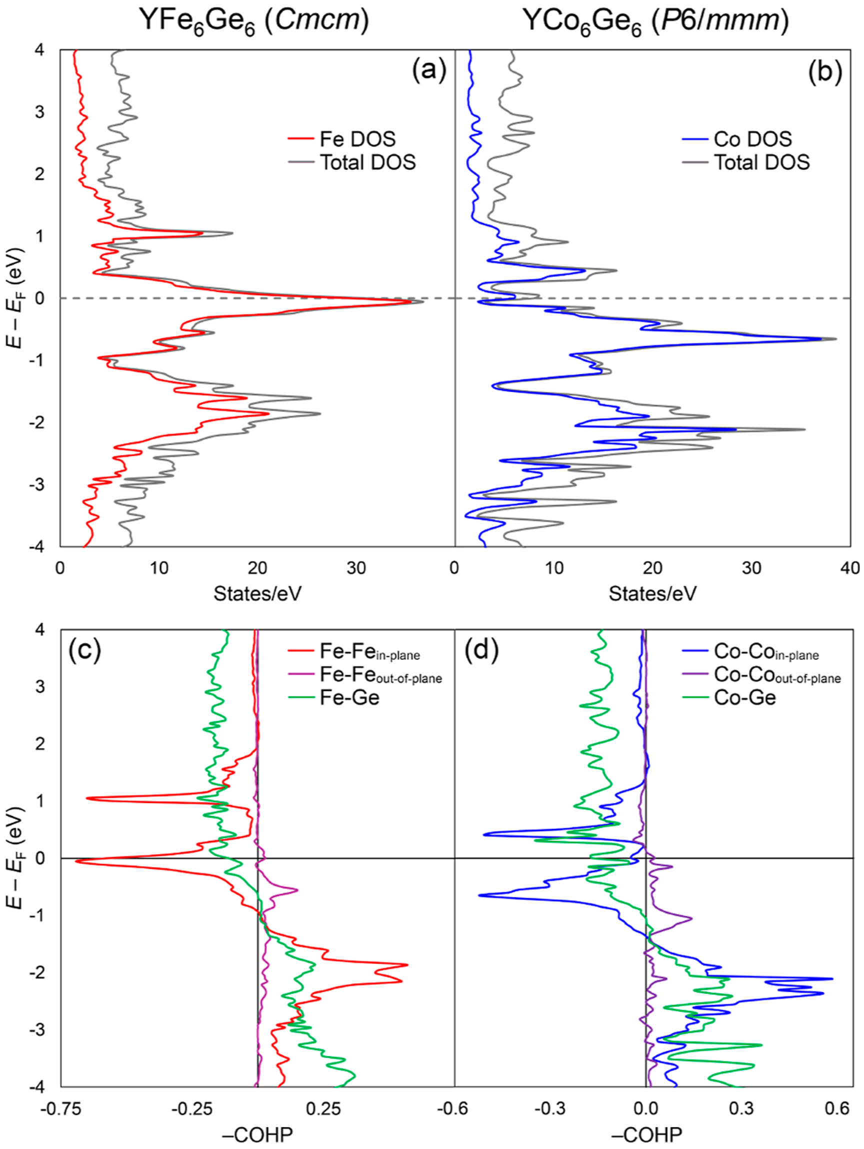

Figure 6. DFT-calculated electronic DOS (a,b) and −COHP (c,d) for YFe_6Ge_6 and YCo_6Ge_6, respectively. The Fermi level coincides with zero of the vertical scale. The Fe−Fe and Co−Co interactions within the kagomé layers are indicated as "in-plane" while the interactions between the layers are indicated as "out-of-plane".

Increase in the concentration of 3d electrons caused by the substitution of Co for Fe should lead to filling of the 3d states and raising of the Fermi level relative to the DOS peak. As a result, in YCo_6Ge_6 the Fermi level appears in a pseudogap above the peak (Figure 6b), suggesting a stable nonpolarized electronic structure. Indeed, the Stoner criterion is not met, with $J{\cdot}N(E_F) < 1$ (Table 2), which explains the PM behavior of this material. The difference in the total calculated energy of a magnetically ordered (FM or AFM) phase and the nonpolarized PM phase clearly reveals the strong preference of YFe_6Ge_6 toward magnetic ordering and the lack of such preference in the case of YCo_6Ge_6 (Table 2). We also note that the total AFM ground state is slightly preferred for YFe_6Ge_6, but the FM ground state is energetically close to the ground state.

The emergence of itinerant magnetism can be also analyzed in terms of crystal orbital Hamilton populations (COHP).[39] It was shown that the magnetic ordering with FM nearest-neighbor interactions correlates with the presence of strongly antibonding states at the Fermi level,[21] which correspond to negative values of the −COHP function. In the electronic structure of YFe_6Ge_6, the Fermi level crosses such antibonding states that correspond to the Fe−Fe interactions within the kagomé layer (Figure 6c). This theoretical picture is in agreement with the magnetic structure of YFe_6Ge_6, where the Fe 3*d* moments exhibit FM in-layer arrangement.[25] In YCo_6Ge_6, this antibonding peak is completely filled (Figure 6d). Thus, neither the Stoner criterion nor the COHP analysis favors magnetic ordering in this material.

■ CONCLUDING REMARKS

The analysis of the DOS and COHP shows that the increase in the Co/Fe ratio, concomitant with the increase in the d-electron count, leads to progressive population of both the large DOS peak observed at E_F and the T−T antibonding states (Figure 6). Therefore, one might expect that the itinerant magnetic ordering in these solids should weaken with a higher Co content. Such an effect, indeed, is observed

https://doi.org/10.1021/acs.chemmater.4c02382
Chem. Mater. 2025, 37, 247−254

experimentally for the $YFe_{6-x}Co_xGe_6$ series, as the magnetic ordering temperature decreases with x (Figure 7). The Fermi level crossing the antibonding states of the COHP function should favor magnetic ordering with the FM nearest-neighbor interactions throughout this series. Therefore, the observed evolution from the overall AFM order for the compositions with $x \leq 3$ toward the FM-like ordering for $x = 4$ and 5, most likely, stems from the decrease in the distance between the kagomé layers, corresponding to the secondary interactions between the transition-metal sites. As a matter of fact, the largest structural changes are observed in the direction perpendicular to the kagomé layers, with the lattice shrinking by ~4% on going from YFe_6Ge_6 to YCo_6Ge_6. Understanding the influence of the in-plane and out-of-plane T−T exchange interactions on the type of magnetic ordering, as well as the role played by the electropositive and main-group elements in mediating those interactions, requires further studies of both the magnetic structure of the $YFe_{6-x}Co_xGe_6$ materials and the structural and magnetic properties of compounds of the "1−6−6" family with the related chemical compositions.

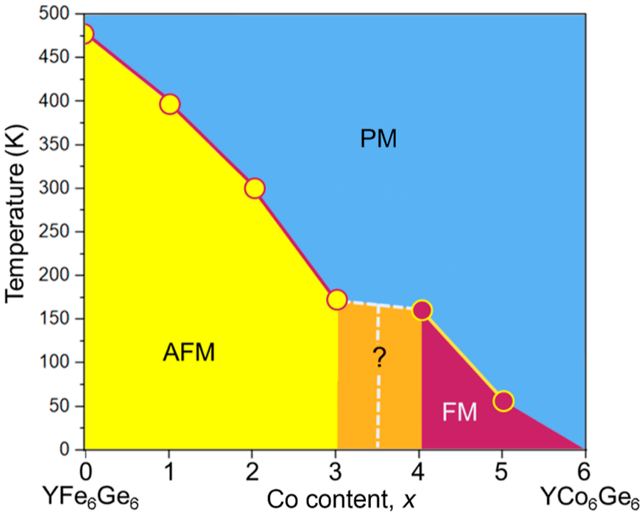

Figure 7. Magnetic phase diagram of $YFe_{6-x}Co_xGe_6$ showing the occurrence of different magnetic regimes as a function of temperature and Co content.

It is also of interest to understand whether the abrupt change in the magnetic behavior happening at the borderline between orthorhombic $YFe_3Co_3Ge_6$ and hexagonal $YFe_2Co_4Ge_6$ (the orange-shaded region in Figure 7) is related to the change in the space-group symmetry of the underlying crystal structure. To that end, our nearest work will focus on exploring the compositional landscape within that narrow region.

Another significant question, certainly worth investigating, deals with the influence of disorder and vacancies in the crystal structures of these materials on the observed magnetic behavior. Different annealing regimes or alternative synthetic methods might lead to the pronounced changes in the magnetic and transport properties. In this vein, the growth of representative single crystals of such 1−6−6-type materials[40] should be invaluable. All the aforementioned problems are currently being researched in our laboratories, and results of those studies will be reported in due course.

■ ASSOCIATED CONTENT

Supporting Information

The Supporting Information is available free of charge at https://pubs.acs.org/doi/10.1021/acs.chemmater.4c02382.

PXRD patterns and unit cell parameters of $YFe_{6-x}Co_xGe_6$ (PDF)

■ AUTHOR INFORMATION

Corresponding Author

Michael Shatruk − *Department of Chemistry and Biochemistry, Florida State University, Tallahassee, Florida 32306, United States*; orcid.org/0000-0002-2883-4694; Email: shatruk@chem.fsu.edu

Authors

Victoria M. Li − *Department of Chemistry and Biochemistry, Florida State University, Tallahassee, Florida 32306, United States*

Milo Adams − *Department of Chemistry and Biochemistry, Florida State University, Tallahassee, Florida 32306, United States*

Complete contact information is available at: https://pubs.acs.org/10.1021/acs.chemmater.4c02382

Author Contributions

The manuscript was written through contributions of all authors. All authors have given approval to the final version of the manuscript.

Funding

This work was supported by the National Science Foundation (Award DMR-2233902 to M.S.). The Quantum Design MPMS-3 system used for magnetic measurements was acquired with support of the NSF MRI program (DMR-2216125).

Notes

The authors declare no competing financial interest.

■ ACKNOWLEDGMENTS

We gratefully acknowledge access to equipment provided by the X-ray Crystallography Center (FSU075000XRAY) and the Materials Characterization Laboratory (FSU075000MAC) at the Department of Chemistry and Biochemistry, Florida State University.

■ ABBREVIATIONS

FM, ferromagnetic; AFM, antiferromagnetic; FiM, ferrimagnetic; PM, paramagnetic; EDX, energy-dispersive X-ray; DFT, density functional theory; DOS, density of states; COHP, crystal orbital Hamilton population.

■ REFERENCES

(1) Syôzi, I. Statistics of Kagomé Lattice. *Prog. Theor. Phys.* **1951**, *6*, 306−308.

(2) Ramirez, A. P. Strongly Geometrically Frustrated Magnets. *Annu. Rev. Mater. Sci.* **1994**, *24*, 453−480.

(3) Richter, J.; Schulenburg, J.; Honecker, A. Quantum Magnetism in Two Dimensions: From Semi-Classical Néel Order to Magnetic Disorder. *Lect. Notes Phys.* **2004**, *645*, 85−153.

(4) Colman, R. H.; Ritter, C.; Wills, A. S. Toward Perfection: Kapellasite, $Cu_3Zn(OH)_6Cl_2$, a New Model $S = 1/2$ Kagome Antiferromagnet. *Chem. Mater.* **2008**, *20*, 6897−6899.

(5) Shores, M. P.; Nytko, E. A.; Bartlett, B. M.; Nocera, D. G. A Structurally Perfect $S = 1/2$ Kagomé Antiferromagnet. *J. Am. Chem. Soc.* **2005**, *127*, 13462−13463.

(6) Balents, L. Spin Liquids in Frustrated Magnets. *Nature* **2010**, *464*, 199−208.

(7) Broholm, C.; Cava, R. J.; Kivelson, S. A.; Nocera, D. G.; Norman, M. R.; Senthil, T. Quantum Spin Liquids. *Science* **2020**, *367*, No. eaay0668.

(8) Snyder, J.; Slusky, J. S.; Cava, R. J.; Schiffer, P. How 'Spin Ice' Freezes. *Nature* **2001**, *413*, 48−51.

(9) Yin, J.-X.; Lian, B.; Hasan, M. Z. Topological Kagome Magnets and Superconductors. *Nature* **2022**, *612*, 647−657.

(10) Shatruk, M.; Adams, M. Rare-Earth Kagomé lattice Materials. In *Handb. Phys. Chem. Rare Earths*; Bünzli, J.-C. G., Kauzlarich, S. M., Eds.; Elsevier, 2023; Vol. *64*, pp 247−280.

(11) Ye, L.; Kang, M.; Liu, J.; von Cube, F.; Wicker, C. R.; Suzuki, T.; Jozwiak, C.; Bostwick, A.; Rotenberg, E.; Bell, D. C.; Fu, L.; Comin, R.; Checkelsky, J. G. Massive Dirac Fermions in a Ferromagnetic Kagome Metal. *Nature* **2018**, *555*, 638−642.

(12) Liu, E.; Sun, Y.; Kumar, N.; Muechler, L.; Sun, A.; Jiao, L.; Yang, S.-Y.; Liu, D.; Liang, A.; Xu, Q.; Kroder, J.; Süß, V.; Borrmann, H.; Shekhar, C.; Wang, Z.; Xi, C.; Wang, W.; Schnelle, W.; Wirth, S.; Chen, Y.; Goennenwein, S. T. B.; Felser, C. Giant Anomalous Hall Effect in a Ferromagnetic Kagome-Lattice Semimetal. *Nat. Phys.* **2018**, *14*, 1125−1131.

(13) Siegfried, P. E.; Bhandari, H.; Jones, D. C.; Ghimire, M. P.; Dally, R. L.; Poudel, L.; Bleuel, M.; Lynn, J. W.; Mazin, I. I.; Ghimire, N. J. Magnetization-Driven Lifshitz Transition and Charge-Spin Coupling in the Kagome Metal YMn_6Sn_6. *Commun. Phys.* **2022**, *5*, 58.

(14) Ghimire, N. J.; Dally, R. L.; Poudel, L.; Jones, D. C.; Michel, D.; Magar, N. T.; Bleuel, M.; McGuire, M. A.; Jiang, J. S.; Mitchell, J. F.; Lynn, J. W.; Mazin, I. I. Competing Magnetic Phases and Fluctuation-Driven Scalar Spin Chirality in the Kagome Metal YMn_6Sn_6. *Sci. Adv.* **2020**, *6*, No. eabe2680.

(15) Shimizu, M. Itinerant Electron Magnetism. *Rep. Prog. Phys.* **1981**, *44*, 329−409.

(16) Duc, N. H.; Brommer, P. E. Formation of 3d-Moments and Spin Fluctuations in Some Rare-Earth-Cobalt Compounds. *Handb. Magn. Mater.* **1999**, *12*, 259−394.

(17) Tan, X.; Tener, Z. P.; Shatruk, M. Correlating Itinerant Magnetism in RCo_2Pn_2 Pnictides (R = La, Ce, Pr, Nd, Eu, Ca; Pn = P, As) to Their Crystal and Electronic Structures. *Acc. Chem. Res.* **2018**, *51*, 230−239.

(18) Landrum, G. A.; Dronskowski, R. The Orbital Origins of Magnetism: From Atoms to Molecules to Ferromagnetic Alloys. *Angew. Chem., Int. Ed.* **2000**, *39*, 1560−1585.

(19) Samolyuk, G. D.; Miller, G. J. Relation between Chemical Bonding and Exchange Coupling Approaches to the Description of Ordering in Itinerant Magnets. *J. Comput. Chem.* **2008**, *29*, 2177−2186.

(20) Shatruk, M. Chemical Aspects of Itinerant Magnetism. In *Encycl. Inorg. Bioinorg. Chem.*; Scott, R. A., Ed.; Wiley VCH: Chichester, 2017; p eibc2494.

(21) Landrum, G. A.; Dronskowski, R. Ferromagnetism in Transition Metals: A Chemical Bonding Approach. *Angew. Chem., Int. Ed.* **1999**, *38*, 1389−1393.

(22) Borgsmiller, L.; Zavanelli, D.; Snyder, G. J. Phase-Boundary Mapping to Engineer Defects in Thermoelectric Materials. *PRX Energy* **2022**, *1*, 022001.

(23) Venturini, G. Filling the CoSn Host-Cell: The $HfFe_6Ge_6$-Type and the Related Structures. *Z. Kristallogr.* **2006**, *221*, 511−520.

(24) Fredrickson, D. C.; Lidin, S.; Venturini, G.; Malaman, B.; Christensen, J. Origins of Superstructure Ordering and Incommensurability in Stuffed CoSn-Type Phases. *J. Am. Chem. Soc.* **2008**, *130*, 8195−8214.

(25) Schobinger-Papamantellos, P.; Buschow, K. H. J.; de Boer, F. R.; Ritter, C.; Isnard, O.; Fauth, F. The Fe Ordering in RFe_6Ge_6 Compounds with Non-Magnetic R (R = Y, Lu, Hf) Studied by Neutron Diffraction and Magnetic Measurements. *J. Alloys Compd.* **1998**, *267*, 59−65.

(26) Fedyna, M. F.; Skolozdra, R. V.; Gorelenko, Y. K. Magnetic and Electric Properties of RCo_6Ge_6 (R = Y, Dy, Er-Lu). *Inorg. Mater.* **1999**, *35*, 373−375.

(27) Venturini, G.; Welter, R.; Malaman, B. Crystallographic Data and Magnetic Properties of RT_6Ge_6 Compounds (R = Sc, Y, Nd, Sm, Gd−Lu; T = Mn, Fe). *J. Alloys Compd.* **1992**, *185*, 99−107.

(28) *X'pert Highscore Plus Software V. 2.2b*; PANalytical B.V.: Almelo, Netherlands, 2006.

(29) Blöchl, P. E. Projector Augmented-Wave Method. *Phys. Rev. B* **1994**, *50*, 17953−17979.

(30) Kresse, G.; Hafner, J. Ab Initio Molecular Dynamics for Liquid Metals. *Phys. Rev. B* **1993**, *47*, 558−561.

(31) Kresse, G.; Joubert, D. From Ultrasoft Pseudopotentials to the Projector Augmented-Wave Method. *Phys. Rev. B* **1999**, *59*, 1758−1775.

(32) Perdew, J. P.; Burke, K.; Ernzerhof, M. Generalized Gradient Approximation Made Simple. *Phys. Rev. Lett.* **1996**, *77*, 3865−3868.

(33) Maintz, S.; Deringer, V. L.; Tchougréeff, A. L.; Dronskowski, R. LOBSTER: A Tool to Extract Chemical Bonding from Plane-Wave Based Dft. *J. Comput. Chem.* **2016**, *37*, 1030−1035.

(34) Buchholz, W.; Schuster, H.-U. Intermetallic Phases with B35-Superstructure and Relationship to $LiFe_6Ge_6$. *Z. Anorg. Allg. Chem.* **1981**, *482*, 40−48.

(35) Cadogan, J. M.; Ryan, D. H.; Swainson, I. P.; Moze, O. The Magnetic Structure of YFe_6Ge_6. *J. Phys.: Condens. Matter* **1998**, *10*, 5383−5388.

(36) Lin, Y.-P.; Liu, C.; Moore, J. E. Complex Magnetic and Spatial Symmetry Breaking from Correlations in Kagome Flat Bands. *Phys. Rev. B* **2024**, *110*, L041121.

(37) Stoner, E. C. Collective Electron Ferromagnetism. *Proc. R. Soc. Ser. A* **1938**, *165*, 372−414.

(38) Janak, J. F. Uniform Susceptibilities of Metallic Elements. *Phys. Rev. B* **1977**, *16*, 255−262.

(39) Dronskowski, R.; Blochl, P. E. Crystal Orbital Hamilton Populations (COHP) - Energy-Resolved Visualization of Chemical Bonding in Solids Based on Density-Functional Calculations. *J. Phys. Chem.* **1993**, *97*, 8617−8624.

(40) Wang, Y.; McCandless, G. T.; Wang, X.; Thanabalasingam, K.; Wu, H.; Bouwmeester, D.; van der Zant, H. S. J.; Ali, M. N.; Chan, J. Y. Electronic Properties and Phase Transition in the Kagome Metal $Yb_{0.5}Co_3Ge_3$. *Chem. Mater.* **2022**, *34*, 7337−7343.